A Mixture-Fraction–Based Hybrid Binomial Langevin–Multiple Mapping Conditioning Model

Andrew P. Wandel[a,b], R. Peter Lindstedt[c]

[a] *University of Southern Queensland,*
Computational Engineering and Science Research Centre,
School of Mechanical and Electrical Engineering,
Toowoomba, 4350, Australia
[b] *Corresponding author. Fax: +61 7 4631 2526; E-mail: andrew.wandel@usq.edu.au*
[c] *Department of Mechanical Engineering,*
Imperial College London,
London, SW7 2BX, UK

Abstract

Generalized Multiple Mapping Conditioning (MMC) allows for the use of any physical quantity to represent the required reference variable provided that it delivers the desired behavior. The binomial Langevin model (BLM) has been shown to predict higher statistical moments with good accuracy. However, joint–scalar modeling for many scalars becomes problematic because scalar bounds must be specified as conditional on other scalars to preserve elemental balances. The resulting volumes in state space become exceptionally complex for realistic problem sizes. In the current work, this central difficulty is avoided by using only velocity and mixture fraction statistics from the BLM with the latter used as the MMC reference variable. The principal advantage of this method is that the implementation of the binomial Langevin mixture fraction is relatively straightforward and provides a direct physical link to MMC. The MMC model is closed using an augmented modified Curl's model where the selection of particle pairs for (turbulent)

mixing ensures proximity in reference space and a corresponding closeness in physical space. The method is evaluated for a lifted methane jet flame undergoing auto-ignition in a vitiated coflow. Most of the major features of the flow are well reproduced and found to generally outperform other modeling approaches, including Large Eddy Simulations using simplified treatments of turbulence–chemistry interactions such as unsteady flamelet/progress variable descriptions.

Keywords: Turbulent combustion, Multiple Mapping Conditioning, MMC, Langevin models, Lifted flame

---

1. Introduction

The desire to combine improved combustion efficiency with lower emissions has led to an increased interest in combustion systems that operate near stability limits. Finite-rate chemistry effects (such as extinction/reignition) become important under such conditions and the formulation of calculation methods capable of reproducing such phenomena has received substantial interest [1, 2, 3, 4]. Time-scales covering several orders of magnitude become important [5] with turbulence typically interacting strongly with chemical kinetics. Simple models cannot capture such phenomena and transported probability density function (PDF) based models are typically required [6, 7]. Predictions are more sensitive to various model components—including the closure for molecular mixing [8]—in such situations.

The hybrid binomial Langevin–Multiple Mapping Conditioning (MMC) model [9, 10] aims to combine some of the benefits of the binomial Langevin model (BLM) [11], such as predictions of higher statistical moments, with the benefits of the MMC approach [12], while overcoming at least some of the deficiencies associated with each individual model component. Previously, the hybrid model utilized a velocity component for mapping the MMC mixture fraction. The current work replaces the velocity with a mixture fraction to provide a more physical basis for general flames.

One of the difficulties with BLM is joint–scalar modeling because the bounds for all scalars must be specified as conditional on all other scalars to conserve elemental balances. A formulation of the joint velocity–scalar PDF that includes the joint statistics of a mixture fraction and a reaction progress variable has been developed [13]. The formulation provides detailed statistics

of velocity–scalar interactions, predicting higher moments with encouraging accuracy. The current hybrid model seeks to retain this ability while averting the central difficulty of evolving (variable) scalar bounds.

In the MMC framework, a mathematical reference space is utilized that has sufficient dimensions in scalar space to describe the manifold on which compositions may lie [14]. This is founded on the principles of ordinary and doubly-conditioned Conditional Moment Closures (CMC) [15] applied in previous studies [16, 17, 18]. The probabilistic approach [19] (similar to second-order CMC) provides an alternative [20], has been implemented in a variety of ways [21, 22, 23], and forms the basis for the MMC component of the current hybrid model.

Surrogate reference variables have been developed for MMC to avoid difficulties in specifying model coefficients: some quantity (preferably already solved as part of the calculation procedure) is used as the reference variable. This is fundamental to the application of generalized MMC [24, 25, 26]. The transformation of such a quantity into a reference variable has been utilized in sparse Lagrangian Large Eddy Simulations (LES) by using the LES-resolved filtered mixture fraction field [24, 27, 28]. In the current hybrid approach, the mixture fraction obtained from BLM is used as the reference variable. The scalar mixing in the MMC component of the hybrid model is then controlled by specifying the fraction of particles which are to be mixed. The model is evaluated by simulating a fuel jet undergoing auto-ignition in a vitiated coflow [29].

2. Theory

2.1. Binomial Langevin model

Hůlek and Lindstedt [13] developed a generalized form of BLM [11] for the joint-PDF of velocity and multiple scalars. The velocity transport model (including the turbulent dissipation ε, the return-to-isotropy of the Reynolds stresses and the dispersion in velocity space) for a stochastic particle p is:

$$du_i^{*p} = \frac{1}{\tau_u}\left(\alpha_1\delta_{ij} + \alpha_2\beta_{ij}\right)\left(u_j^{*p} - \langle u_j\rangle\right)dt + (C_0\langle\varepsilon\rangle)^{1/2}dw_i \tag{1}$$

where superscript '$*$' represents a stochastic trajectory, k is the turbulent kinetic energy, the velocity time–scale is $\tau_u = \langle k\rangle/\langle\varepsilon\rangle$, dw_i is an isotropic Wiener process and the Reynolds stress anisotropy tensor is

$$\beta_{ij} = \frac{\langle u_i' u_j'\rangle}{\langle u_k' u_k'\rangle} - \frac{\delta_{ij}}{3}\,. \tag{2}$$

The modeling coefficients are $C_0 = 2.1$, $\alpha_2 = 3.7$ and $\alpha_1 = -\left(\frac{1}{2} + \frac{3}{4}C_0\right) - \alpha_2\beta_{ll}^2$. The modeled stochastic differential equation for any scalar η is

$$d\eta^{*p} = \frac{G_\eta}{2\tau_\eta}\left(\eta^{*p} - \langle\eta\rangle\right)dt + \left(B_\eta\langle\varepsilon_\eta\rangle\right)^{1/2}dw_{\text{bin}} \tag{3}$$

where the drift (G_η) and diffusion (B_η) coefficients are defined elsewhere [11, 13], dw_{bin} is a binomial Wiener process [11] and the mean scalar dissipation is modeled as $\langle\varepsilon_\eta\rangle \equiv \langle\eta'^2\rangle/\tau_\eta$, with the scalar timescale modeled using the timescale ratio C_ϕ:

$$\tau_\eta = \tau_u/C_\phi\,. \tag{4}$$

Many of the physical processes that occur are simulated well by the model [13]. However, the presence of conditional scalar limits in G_η and

B_η for reacting scalars cause difficulties due to evolving scalar bounds. This issue has been addressed for a two–scalar formulation by ensuring transport along a scalar boundary for limiting cases [13]. Generally, a much larger number of scalars (e.g. 48 species in the current case) must be considered, resulting in very complex volumes in composition space. However, if the implementation is restricted to the mixture fraction alone (where the bounds are simple), then no difficulties arise.

2.2. MMC model

The current work utilizes Generalized MMC [26], so does not solve the standard transport equation for the reference variable (ξ^{*p}) [12], because the mixture fraction solved by the binomial Langevin model is defined to be the reference variable:

$$\xi^{*p} = \eta^{*p} \,. \tag{5}$$

Instead, the transport of the reference variable is solved by Eq. (3). The same particle contains information from both the BLM and MMC, so η directly maps to the MMC mixture fraction Z. The major benefits of this approach are that the reference variable does not merely map, but actually models the behavior of the mixture fraction; and the inhomogeneous drift term, which is challenging to model, does not need to be determined.

Equation (5) is the principal difference with the previous hybrid binomial Langevin–MMC model [9, 10]; previously the velocity from Eq. (1) was used to define ξ in Eq. (5). Because η was used in the earlier work to control the amount of mixing, another model for the mixing needs to be implemented, which will be discussed later.

In the MMC framework, n_s reactive scalars are solved with $n_s - 1$ species mass fractions (Y_I) combined with the specific enthalpy h. The stochastic form of the transport equations is [12]:

$$dZ^{*p} = S dt \tag{6}$$

$$dY_I^{*p} = (S + W_I) dt \tag{7}$$

$$d\mathbf{x}^{*p} = \mathbf{U} dt \,. \tag{8}$$

Here, S is the mixing model, W_I the chemical source term, dw_l a Wiener process and $\mathbf{U} \equiv \langle \mathbf{v} | \boldsymbol{\xi} \rangle$ the conditional velocity, with $\mathbf{v}$ the physical velocity. To ensure compatibility with the joint-PDF of mixture fraction and velocity for BLM, the BLM velocity obtained from Eq. (1) is used in Eq. (8) for the current hybrid model:

$$\mathbf{U} = \mathbf{u} \,. \tag{9}$$

The conventional model for the diffusion coefficient B was used

$$B = \frac{\langle \varepsilon_\eta \rangle}{2} \left\langle \left(\frac{\partial Z}{\partial \xi} \right)^2 \right\rangle^{-1} , \tag{10}$$

with the derivative obtained by subdividing the reference space and performing least-squares curve fits in each section [30].

The Modified Curl's (MC) model [31, 32] was applied for the mixing term (S). What distinguishes MMC from MC is that pairs of particles are not randomly paired, which could cause interaction across a diffusion layer (which would only happen in extremely high turbulence). Instead pairs of particles are selected to be close in reference space, modeling the behavior that particles are physically close together (at a subgrid scale) because the mapping process requires the reference variable to change across a diffusion layer in

a similar way to the mixture fraction. Particles are considered available for pairing according to [10, 30]

$$|\Delta\xi^{*pq}| \leq (2B\Delta t)^{1/2} \tag{11}$$

where $\Delta\xi^{*pq} = \xi^{*q} - \xi^{*p}$. This mimics the effect of the diffusive term of a stochastic differential equation [i.e. the last term of Eq. (1) or Eq. (3)], where the average distance particles diffuse is $(2B\Delta t)^{1/2}$ and the particles interact at the new location. To reduce the chances of Eq. (11) being violated, p is selected so that $|\xi^{*p}|$ is in descending order. If no q can be found to satisfy Eq. (11), then q is selected to minimize $|\Delta\xi^{*pq}|$ and any violation will occur for outliers, which are in the low-probability region. In common with all other PDF-based approaches where particles mix by sharing information with a small number of particles (usually one other), if Δt is too small or the number of particles is insufficient (i.e. if $n_p\Delta t \to 0$, where n_p is the number of particles in a physical cell), then the model fails ($\langle Z''^2\rangle$ does not decay in the mixing substep).

Particles are paired with a nearby particle, not the neighboring particle. The reason for this is that smaller values of $n_p\Delta t$ are possible without changing the result. Those MMC methods which pair neighboring particles, e.g. [33, 21], rely on sufficiently-high values of $n_p\Delta t$ to reorder the particles so particles do not uniquely pair with the same particle repeatedly. Such behavior is also observed in the stranding behavior of EMST if it is implemented without the aging function, which causes many of the particles to be unavailable for interactions. Arguably, the low $n_p\Delta t$ limit of MMC behaves worse than EMST in terms of stranding: MMC is restricted to isolated pairs of particles, whereas in EMST interactions can occur between multiple par-

ticles. The method used here and in related work [9, 10, 20, 30] guarantees dissipation in the mixing process for smaller values of $n_p \Delta t$ than methods that pair neighboring particles. Because the distance between particles in reference space is consequentially greater for individual particles than if they were neighboring, the amount of dissipation per mixing interaction and the number of paired particles must also be different.

To close the model for S, the MC model [31, 32] was used. The process of choosing the degree of mixing differs from the previous model because η is not available for controlling this process. For those particles selected for mixing, the amount of mixing was 50% [30] of that specified in the original Curl's model. The number of particles selected for mixing remains an unclosed parameter. In the current work, 6% of particles at any physical location were mixed per time step; on average, this amounted to 24 particles. It is likely that this value of 6% is not general and future work will focus on a general approach to selecting the number of particles to mix.

The method of mixing follows the same procedure as standard MC. Firstly, the method for choosing pairs must be decided. In MC, particles are randomly chosen from the available set of particles (normally those within a computational cell, so the particles are moderately close in physical space). In the current method, the pair for a particle is chosen at random from the subset of particles within the computational cell that are also close in reference space. Secondly, the distribution of the mixing amount must be chosen. A uniform distribution is common for MC (the amount of mixing is a uniformly-distributed random variable between no mixing and complete mixing). The current method specifies a single value that provides the same

mean amount of mixing [30]; modifying this to a random value affects the conditional means [30]. Finally, the fraction of particles to be mixed must be determined. In MC, this is governed by the distribution of the mixing amount and the rate of decay of scalar variance. A fixed value is used here for simplicity, but this can be replaced to allow variations.

3. Results

3.1. Simulated experiment

The experiment [29] studied here is a methane-air jet (CH_4 33% v.v.) with a velocity of 100 m/s and pipe diameter of 4.57 mm (jet $\mathrm{Re} = 28,000$). The coflow was air vitiated with H_2 (lean: $\Phi = 0.40$) and burned prior to being released as coflow at 5.4 m/s and 1350 K. The typical behavior of this setup is a lifted flame where the liftoff height is very sensitive to the inflow speeds and temperature. This case is challenging for models because predicting the liftoff behavior accurately requires suitable treatment of extinction/reignition behavior.

The model was implemented into a parabolic code used successfully in a previous study of the current vitiated flow [34]. In each simulation, there were 80 cells in the radial direction, with the width of the domain increasing as the entrained region grew. There was also variable spacing in the axial direction, with $\Delta z/d = 1.5\times10^{-3}$ initially, linearly increasing to $\Delta z/d = 0.05$ at $z/d = 10$, then subsequently linearly increasing up to $\Delta z/d = 0.11$ in the range $30 < z/d < 60$. On average, 400 particles were used in each cell, with an ensemble of 10 simulations. Direct integration of the chemistry was used in order to eliminate interpolation errors. The reduced chemical mechanism

comprises 48 species (28 in steady-state) and 300 reactions [7].

3.2. Mean statistics

The mean statistics were averaged over a spatial resolution of $\Delta z/d = 0.5$, with no spatial averaging in the radial direction, then averaged over the ensemble. The ensemble standard deviation is computed from the Favre mean from each of the 10 simulations in the ensemble. The centerline mean mixture fraction (Fig. 1) and temperature (Fig. 2) show good agreement for most of the domain, generally reproducing the behavior near the outlet and the axial stabilization point of the lifted flame. From the small ensemble standard deviation in all the results, 400 particles/cell appears to be sufficient to resolve the flow. The centerline rms mixture fraction (Fig. 3) tends to be under-predicted downstream, which is likely due to excessive mixing in this region, but the location and magnitude of the maximum is reproduced. The temperature rms (Fig. 4) is well reproduced for $z/d < 70$, which accounts for most of the important features of the flow. The temperature rms is predicted significantly better than other models [29]. The species centerline distributions are all generally well predicted, with the O_2, OH and CO profiles shown in Fig. 5. Further species are included in the Supplemental Material.

The radial profiles of mean mixture fraction (Fig. 6) and mean temperature (Fig. 7) generally agree with the experimental data. The radial locations of the local maxima in the temperature around the base of the lifted flame ($40 \leq z/d \leq 50$) are predicted well, as is the edge of the coflow. Like the centerline results, the standard deviations tend to be modestly underpredicted.

Most results presented so far are similar to those obtained using the MC model [34]. The exception is the centerline temperature rms, where the au-

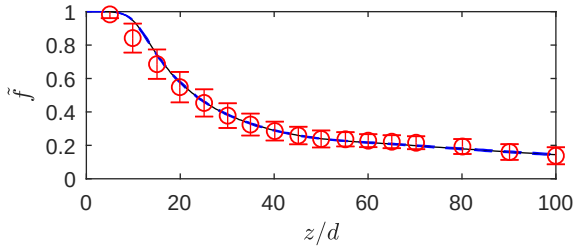

Figure 1: Centerline Favre-average mixture fraction. Hybrid model: ensemble mean, —; ensemble std either side of ensemble mean, – –. Experiment [29], ○.

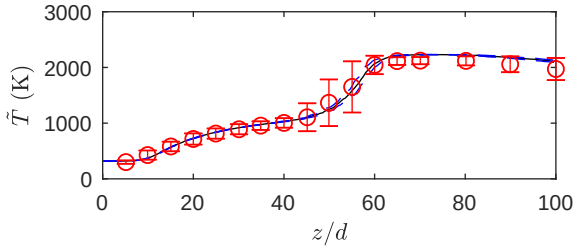

Figure 2: Centerline Favre-average temperature. As per Fig. 1.

thors have not found a RANS simulation that can correctly predict the locations of both the rise at $z/d \simeq 40$ and the decrease at $z/d \simeq 60$. Of the LES simulations that report the temperature rms, some cannot simultaneously predict both these locations [35, 36]. Others that do predict the centerline temperature rms cannot predict a local maxima in the radial profile of mean

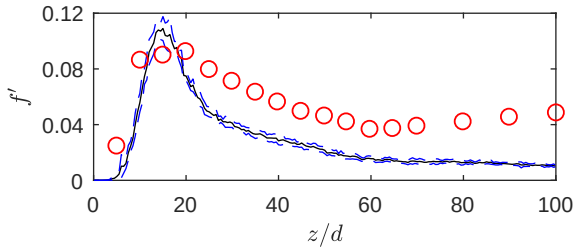

Figure 3: Centerline rms mixture fraction. As per Fig. 1.

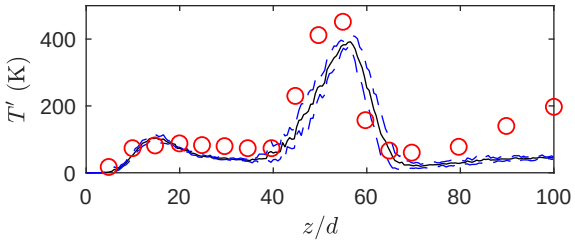

Figure 4: Centerline rms temperature. As per Fig. 1.

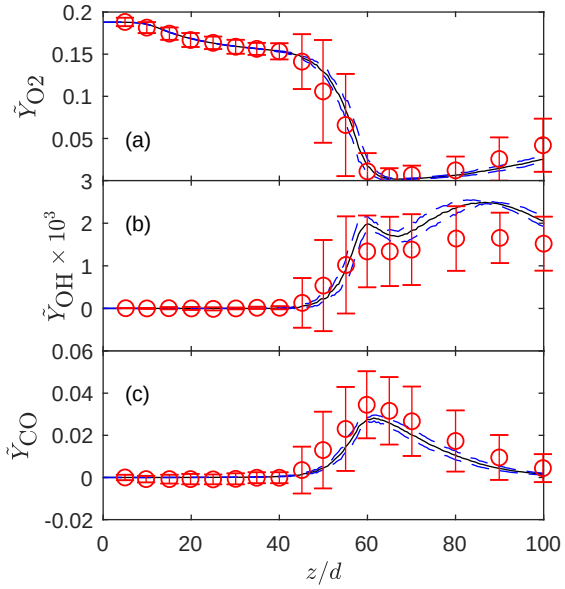

Figure 5: Centerline Favre-average mass fractions. (a) O_2; (b) OH; (c) CO. As per Fig. 1.

temperature at $z/d = 40$ [37, 38].

3.3. Conditional statistics

To properly understand the conditional statistics, the mixture fraction PDF is reported in Fig. 8. The general shape of the experiment is reproduced; the δ-function at $f = 0$ shows that the coflow is resolved throughout the domain; while the maximum mixture fraction decays with distance

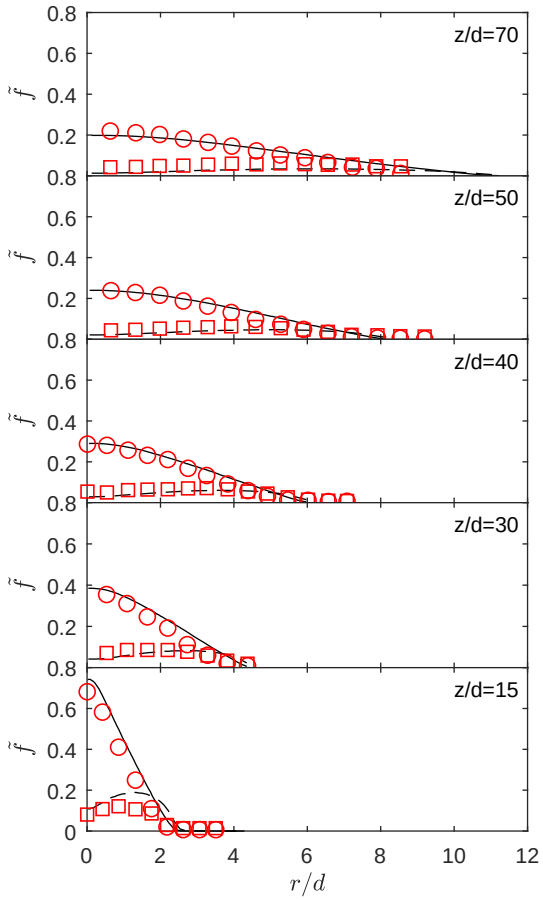

Figure 6: Radial mixture fraction at different axial locations. Hybrid model: mean, —; rms, – –. Experiment [29]: mean, ○; rms, □.

downstream somewhat faster than the experiment, which causes the slight underprediction of the standard deviation.

The scatter plots of temperature with respect to mixture fraction (Fig. 9) show that there is broad agreement with the experimental data. The results presented here are qualitatively similar to the corresponding MC results [34]. The major difference is that by localizing the mixing, the particles tend to be richer for the same temperature, in closer agreement with experiment.

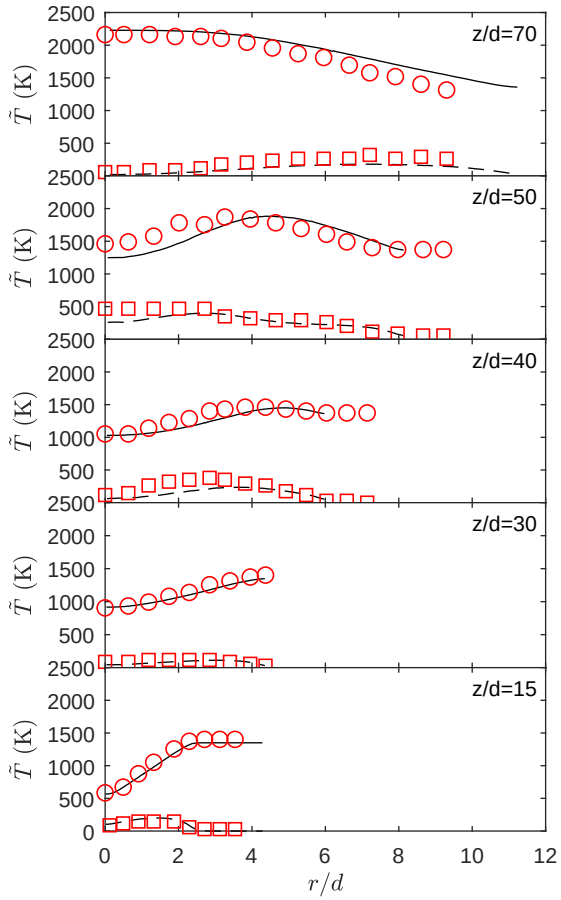

Figure 7: Radial temperature at different axial locations. As per Fig. 6.

Comparing to other computational results [29], for $z/d \leq 40$ there are frozen particles across most of the range of mixture fraction, in line with the experiments. At $z/d = 30$, no particles are close to equilibrium, unlike other studies. There is notable divergence between experimental data and all previous studies at $z/d = 40$. The current results and past MC results [29, 34] appear similar at $z/d = 50$ and reproduce the band of particles at stoichiometric-to-rich mixture fractions which span the frozen and equi-

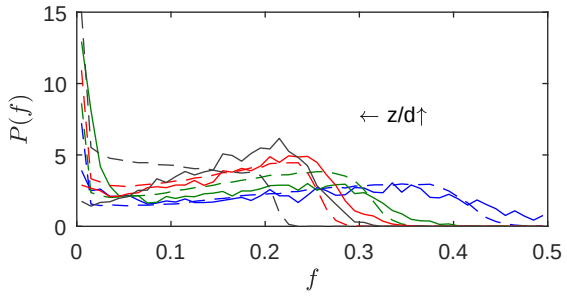

Figure 8: Mixture fraction PDFs. Hybrid model, – –; experiment [29], —. $z/d = 30$, —; 40, —; 50, —; 70, —.

librium limits. However, unlike the MC results [29, 34], local extinction is limited at $z/d = 70$, resulting in better agreement with the experimental data.

Conditional averaging of these results (Fig. 10) shows that the current approach predicts the near-frozen nature of the flow at $z/d = 30$, while repeating the MC model behaviour [29] of the conditional mean being the equilibrium temperature for a large portion of the lean part of the domain further downstream. The lean portion (the stoichiometric mixture fraction is 0.177 [29]) is predicted well by the current model, while other studies over-predict the temperature in this region [29]. Following this trend, the current results under-predict the conditional temperature for the rich region (particularly at $z/d = 50$) in contrast to other studies [29]. The behavior of MMC in the rich region can be attributed to the lower centerline mixture fraction rms. Ironically, the latter creates a good prediction at $z/d = 70$, where the MMC results slightly over-predict the experiment for the entire range of mixture fractions. Conditional statistics for some species are included in the Supplemental Material and tend to mirror the predictions of temperature.

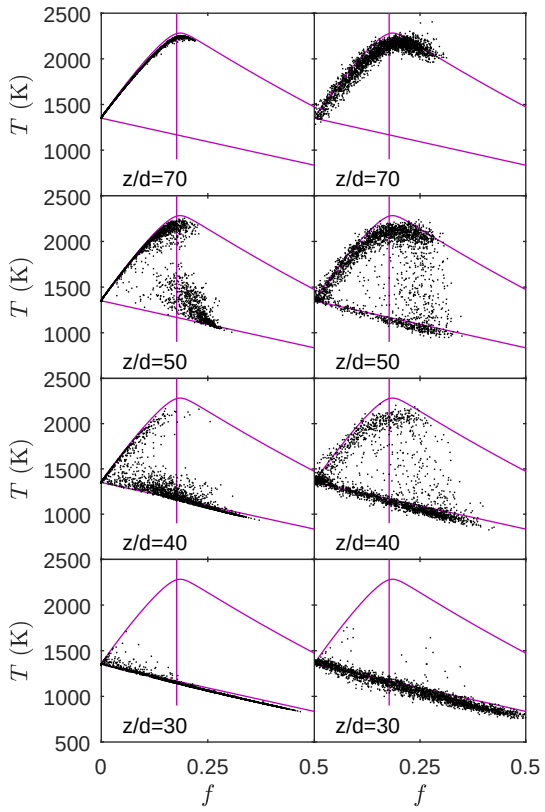

Figure 9: Scatter plots of temperature versus mixture fraction for the hybrid model (left) and experiment [29] (right). There are 2500 randomly-selected data points shown for each axial location. Equilibrium (upper) and frozen (lower) limits, and stoichiometric mixture fraction (vertical line): —.

3.4. Flame liftoff height

The flame liftoff height was calculated by averaging the axial locations where the mole fraction of C_2H_4 reached 100 ppm and C_2H_2 reached 2 ppm [29]. For the base conditions, the liftoff height was found to be $H/D = 42$, somewhat larger than the experimental value of 35 [29]. Similar to previous results [29], there is little sensitivity to coflow velocity (Fig. 11), although the

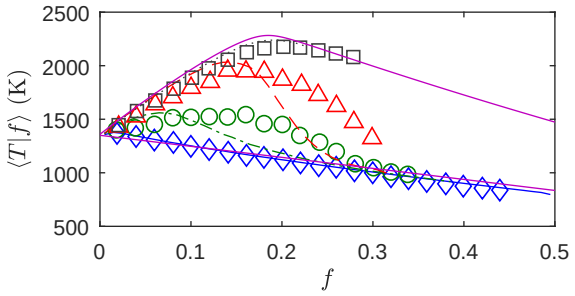

Figure 10: Temperature conditioned on mixture fraction. Hybrid model: $z/d = 30$, —; 40, – ·; 50, – –; 70, · · · . Experiment [29]: $z/d = 30$, ◇; 40, ○; 50, △; 70, □. Equilibrium (upper) and frozen (lower) limits: —.

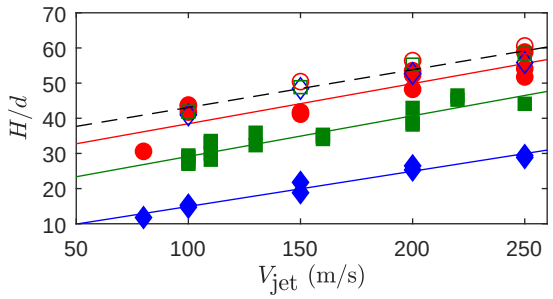

Figure 11: Liftoff height as function of jet velocity. Coflow velocity: 4.2 m/s, ◇; 5.3 m/s, □; 6.5 m/s, ○. Hybrid model: open symbols with linear curve-fit of all results, – –. Experiment [29]: closed symbols with linear curve-fit of each coflow velocity, —.

current results predict a much larger liftoff height. The general trend of a monotonic decrease in liftoff height with increasing coflow temperature is reproduced (Fig. 12), with a lower sensitivity of liftoff height to coflow temperature, consistent with the MC model results using the same code [34]. The insensitivity to coflow conditions could be caused by the mixing model and future improvements may contribute to a greater sensitivity to coflow conditions.

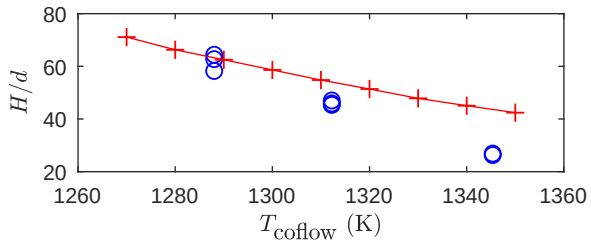

Figure 12: Liftoff height as function of coflow temperature. Hybrid model, +. Experiment [29], ∘.

4. Conclusions

A modified version of the hybrid binomial Langevin–Multiple Mapping Conditioning model has been proposed with the reference variable modeled by the mixture fraction from BLM. This approach promises to improve upon the applicability of the previous formulation [9, 10], while resulting in a simpler implementation. The development of a universal methodology that imposes a physical condition on the fraction of particles to be mixed remains desirable. However, it appears that the current augmented MC model, which imposes local mixing of particles in reference space, removes the tendency of the standard MC model to over-predict local extinction. The model was evaluated for a lifted jet flame [29], with the results generally comparing favorably with experimental data and previous modeling efforts.

Acknowledgments

The current work was, in part, performed at Imperial College while Dr Wandel was on sabbatical. The authors are grateful to Mr P. Simatos for technical support in conducting the simulations.

References

[1] G. Coppola, B. Coriton, A. Gomez, Combust. Flame 156 (2009) 1834–1843.

[2] Y. Shoshin, J. Jarosinski, Proc. Combust. Inst. 32 (2009) 1043–1050.

[3] U. Do Lee, C.S. Yoo, J.H. Chen, J.H. Frank, Proc. Combust. Inst. 32 (2009) 1059–1066.

[4] S. Delhaye, L.M.T. Somers, J.A. van Oijen, L.P.H. de Goey, Proc. Combust. Inst. 32 (2009) 1051–1058.

[5] N. Peters, Proc. Combust. Inst. 32 (2009) 1–25.

[6] S.B. Pope, Combust. Flame 27 (1976), 299–312.

[7] R. Lindstedt, S. Louloudi, J. Driscoll, V. Sick, Flow, Turb. Combust. 72 (2004) 407–426.

[8] Z. Ren, S.B. Pope, Combust. Flame 136 (2004) 208–216.

[9] A.P. Wandel, R.P. Lindstedt, Phys. Fluids 21 (2009) 015103.

[10] A.P. Wandel, R.P. Lindstedt, Proc. Combust. Inst. 34 (2013) 1365–1372.

[11] L. Valiño, C. Dopazo, Phys. Fluids A 3 (12) (1991) 3034–3037.

[12] A.Y. Klimenko, S.B. Pope, Phys. Fluids 15 (7) (2003) 1907–1925.

[13] T. Hůlek, R.P. Lindstedt, Combust. Sci. Tech. 136 (1998) 303–331.

[14] S.B. Pope, Flow, Turb. Combust. 72 (2004) 219–243.

[15] A.Y. Klimenko, R.W. Bilger, Prog. Energy Combust. Sci. 25 (6) (1999) 595–687.

[16] M.J. Cleary, A. Kronenburg, Proc. Combust. Inst. 31 (2007) 1497–1505.

[17] M.J. Cleary, A. Kronenburg, Combust. Flame 151 (2007) 623–638.

[18] K. Vogiatzaki, A. Kronenburg, M.J. Cleary, J.H. Kent, Proc. Combust. Inst. 32 (2009) 1679–1685.

[19] A.Y. Klimenko, in: Clean Air, Vol. 7, 2003, p. 14.4.

[20] A.P. Wandel, A.Y. Klimenko, Phys. Fluids 17 (12) (2005) 128105.

[21] C. Straub, S. De, A. Kronenburg, K. Vogiatzaki, Combust. Theory Modelling 20 (5) (2016) 894–912.

[22] A. Varna, M.J. Cleary, E.R. Hawkes, Combust. Flame 181 (2017) 342–353.

[23] A. Varna, M.J. Cleary, E.R. Hawkes, Combust. Flame 181 (2017) 354–364.

[24] M.J. Cleary, A.Y. Klimenko, Flow, Turb. Combust. 82 (2009) 477–491.

[25] M.J. Cleary, A.Y. Klimenko, in: T. Echekki, E. Mastorakos (Eds.), Turbulent Combustion Modeling, Springer, 2011, pp. 143–173.

[26] K. Ghai, S. De, K. Vogiatzaki, M.J. Cleary, in: S. De, A.K. Agarwal, S. Chaudhuri, S. Sen (Eds.), Modeling and Simulation of Turbulent Combustion, Energy, Environment, and Sustainability, Springer, Singapore, 2018, pp. 447–474.

[27] B. Sundaram, A.Y. Klimenko, M.J. Cleary, Y. Ge, Combust. Theory Modelling 20 (4) (2016) 735–764.

[28] S.Vo, O.T. Stein, A. Kronenburg, M.J. Cleary, Combust. Flame 179 (2017) 280–299.

[29] R. Cabra, J.-Y. Chen, R.W. Dibble, A.N. Karpetis, R.S. Barlow, Combust. Flame 143 (2005) 491–506.

[30] A.P. Wandel, Combust. Theory Modelling 17 (4) (2013) 707–748.

[31] C. Dopazo, Phys. Fluids 22 (1979) 20.

[32] J. Janicka, W. Kolbe, W. Kollmann, J. Non-Equilib. Thermodyn. 4 (1) (1979) 47–66.

[33] B. Sundaram, A.Y. Klimenko, Proc. Combust. Inst. 36 (2017) 1937–1945.

[34] K. Gkagkas, R.P. Lindstedt, Proc. Combust. Inst. 31 (2007) 1559–1566.

[35] M. Ihme, Y.C. See, Combust. Flame 157 (2010) 1850–1862.

[36] O. Schulz, T. Jaravel, T. Poinsot, B. Cuenot, N. Noiray, Proc. Combust. Inst. 36 (2017) 1637–1644.

[37] P. Domingo, L. Vervisch, D. Veynante, Combust. Flame 152 (2008) 415–432.

[38] N. Enjalbert, P. Domingo, L. Vervisch, Combust. Flame 159 (2012) 336–352.

Figure Captions

Figure 1: Centerline Favre-average mixture fraction. Hybrid model: ensemble mean, —; ensemble std either side of ensemble mean, – –. Experiment [29], ○.

Figure 2: Centerline Favre-average temperature. As per Fig. 1.

Figure 3: Centerline rms mixture fraction. As per Fig. 1.

Figure 4: Centerline rms temperature. As per Fig. 1.

Figure 5: Centerline Favre-average mass fractions. (a) O_2; (b) OH; (c) CO. As per Fig. 1.

Figure 6: Radial mixture fraction at different axial locations. Hybrid model: mean, —; rms, – –. Experiment [29]: mean, ○; rms, □.

Figure 7: Radial temperature at different axial locations. As per Fig. 6.

Figure 8: Mixture fraction PDFs. Hybrid model, – –; experiment [29], —. $z/d = 30$, —; 40, —; 50, —; 70, —.

Figure 9: Scatter plots of temperature versus mixture fraction for the hybrid model (left) and experiment [29] (right). There are 2500 randomly-selected data points shown for each axial location. Equilibrium (upper) and frozen (lower) limits, and stoichiometric mixture fraction (vertical line): —.

Figure 10: Temperature conditioned on mixture fraction. Hybrid model: $z/d = 30$, —; 40, – ·; 50, – –; 70, · · · . Experiment [29]: $z/d = 30$, ◇; 40, ○; 50, △; 70, □. Equilibrium (upper) and frozen (lower) limits: —.

Figure 11: Liftoff height as function of jet velocity. Coflow velocity: 4.2 m/s, ◇; 5.3 m/s, □; 6.5 m/s, ○. Hybrid model: open symbols with linear curve-fit of all results, – –. Experiment [29]: closed symbols with linear curve-fit of each coflow velocity, —.

Figure 12: Liftoff height as function of coflow temperature. Hybrid model, +. Experiment [29], ∘.

List of Supplemental Material

Figure S1: Centerline Favre-average CO_2 mass fraction. Hybrid model: ensemble mean, —; ensemble std either side of ensemble mean, – –. Experiment [29], ○.

Figure S2: Centerline Favre-average CH_4 mass fraction. Hybrid model: ensemble mean, —; ensemble std either side of ensemble mean, – –. Experiment [29], ○.

Figure S3: Centerline Favre-average H_2 mass fraction. Hybrid model: ensemble mean, —; ensemble std either side of ensemble mean, – –. Experiment [29], ○.

Figure S4: Centerline Favre-average H_2O mass fraction. Hybrid model: ensemble mean, —; ensemble std either side of ensemble mean, – –. Experiment [29], ○.

Figure S5: Scatter plots of temperature versus mixture fraction (2500 randomly-selected data points shown for each axial location). Equilibrium (upper) and frozen (lower) limits, and stoichiometric mixture fraction (vertical line): —.

Figure S6: Temperature conditioned on mixture fraction. Hybrid model: $z/d = 30$, —; 40, – ·; 50, – –; 70, · · ·. Experiment [29]: $z/d = 30$, ◇; 40, ○; 50, △; 70, □. Equilibrium (upper) and frozen (lower) limits: —.

Figure S7: Rms of conditional temperature. Hybrid model: $z/d = 30$, —; 40, – ·; 50, – –; 70, · · ·. Experiment [29]: $z/d = 30$, ◇; 40, ○; 50, △; 70, □.

Figure S8: Scatter plots of O_2 mass fraction versus mixture fraction for the hybrid model (left) and experiment [29] (right). There are 2500 randomly-selected data points shown for each axial location. Equilibrium

(lower) and frozen (upper) limits, and stoichiometric mixture fraction (vertical line): —.

Figure S9: O_2 mass fraction conditioned on mixture fraction. Hybrid model: $z/d = 30$, —; 40, – ·; 50, – –; 70, · · · . Experiment [29]: $z/d = 30$, ♢; 40, ○; 50, △; 70, □. Equilibrium (lower) and frozen (upper) limits: —.

Figure S10: Rms of conditional O_2 mass fraction. Hybrid model: $z/d = 30$, —; 40, – ·; 50, – –; 70, · · · . Experiment [29]: $z/d = 30$, ♢; 40, ○; 50, △; 70, □.

Figure S11: Scatter plots of OH mass fraction versus mixture fraction for the hybrid model (left) and experiment [29] (right). There are 2500 randomly-selected data points shown for each axial location. Equilibrium, and stoichiometric mixture fraction (vertical line): —.

Figure S12: OH mass fraction conditioned on mixture fraction. Hybrid model: $z/d = 30$, —; 40, – ·; 50, – –; 70, · · · . Experiment [29]: $z/d = 30$, ♢; 40, ○; 50, △; 70, □. Equilibrium: —.

Figure S13: Rms of conditional OH mass fraction. Hybrid model: $z/d = 30$, —; 40, – ·; 50, – –; 70, · · · . Experiment [29]: $z/d = 30$, ♢; 40, ○; 50, △; 70, □.